



Atomic-scale imaging of polyvinyl alcohol crystallinity using electron ptychography

Botao Hao, Zhiyuan Ding, Xudong Tao, Peter D. Nellist^{**}, Hazel E. Assender^{*}

Department of Materials, University of Oxford, Parks Road, OX1 3PH, Oxford, United Kingdom

ARTICLE INFO

Keywords:

Polyvinyl alcohol
Scanning transmission electron microscopy
4D STEM
Electron ptychography

ABSTRACT

Polyvinyl alcohol (PVA) is considered to have great potential in medical, pharmaceutical, and packaging applications because of its outstanding biocompatibility, water solubility, low density and relatively low cost. PVA crystallinity, central to the materials properties, has been studied by X-ray diffraction, but two possible crystal structures are mooted. Electron microscopic techniques can potentially image PVA at high resolution. Still, it is challenging for conventional electron microscopies because of the relatively low crystallinity of PVA, its severe beam sensitivity, and the poor contrast of light elements. Electron ptychography makes use of a 4D STEM dataset comprising the intensity in the STEM detector plane recorded as a function of each probe position and has lower sample damage and better phase-contrast compared to traditional techniques. Here, we use electron ptychography to image PVA crystallinity. The reconstructed images, which show good agreement in the unit cell dimension with X-ray diffraction data, can show how the atoms order in the materials, however, deviations from previous models derived from X-ray diffraction are observed. To interpret the data, we propose a series of changes based on previous models to formulate a description of PVA crystal structure. Simulated results from this new model accord well with the experimental images. This study manages to image both carbon and oxygen atoms in PVA, which has not previously been achieved by any conventional method. The results are expected to bring a new and deeper understanding of PVA crystal structure, and illustrate the opportunity presented by this approach for directly imaging molecular order in polymer crystals.

1. Introduction

Polyvinyl alcohol (PVA) is a polyhydric synthetic polymer containing secondary hydroxyl groups on alternate carbon atoms [1]. Due to its great biocompatibility, high water solubility and chemical resistance, PVA has become one of the most commercially important polymers in use [2]. For example, this material has been widely used in eye drops and soft contact lenses [3]. However, long-term hydrogel mechanical stability of PVA needs extensive and intensive research for some rigorous applications, for instance, artificial cartilage and meniscus [4]. Crystallization is related to mechanical properties of materials, particularly for organics [5], as well as other physical properties such as solubility and diffusion coefficients, density, and tribological and optical properties [6,7]. The crystal structure of PVA is not well-established, and therefore, studying the precise crystal structure can be helpful for tailoring PVA for broader and deeper applications.

Two different diffraction-based PVA crystal models were generated

by Bunn in 1948 [8] and by Sakurada *et al.* in 1950 [9]. These two models as viewed along the [010] direction (along the molecular axis) are shown in Fig. 1. Both models follow the primitive monoclinic crystal system. The basic unit cell parameters of Bunn's model ($a = 0.781$ nm, $b = 0.252$ nm, $c = 0.551$ nm, $\alpha = \gamma = 90^\circ$, $\beta = 91.7^\circ$) [8] and Sakurada's model ($a = 0.783$ nm, $b = 0.252$ nm, $c = 0.553$ nm, $\alpha = \gamma = 90^\circ$, $\beta = 87.0^\circ$) [9] are close, and the discrepancy between two models comes from the way they arrange intermolecular hydrogen bonding. The nature of this intermolecular bonding has been shown key to many properties of PVA [10–12]. There are many possible orientations for inter- and intra-molecular hydrogen bonding within the broad crystal structure [13], and indeed the possibility that water, present during crystallization, may be incorporated within the crystal structure has been suggested [14]. The two original models determined using XRD may not fully describe the practical structure, and a new technique is required for more precise studies. In particular, a high-resolution microscopic technique can potentially image the local features of a single crystallite,

^{*} Corresponding author.

^{**} Corresponding author.

E-mail address: hazel.assender@materials.ox.ac.uk (H.E. Assender).

contributing to the direct observation of PVA crystal information.

Transmission electron microscopy (TEM) is a powerful imaging technique providing atomic-scale structural information of samples. However, there are still three main challenges to using TEM to image PVA. First, PVA is semi-crystalline, and the degree of crystallinity can be very low for the samples, so it can be challenging to find crystals to image using electron microscopy. For this point, some papers reported that freeze-thawing can increase the degree of crystallinity to a certain level [15–17]. Moreover, Assender and Windle [18] found that annealing can be another effective way to further crystallise PVA. Freeze-thawing and annealing, therefore, could be two effective methods to prepare highly crystalline PVA samples for TEM. Secondly, imaging light elements, such as oxygen and carbon, is challenging. This is because light atoms with low atomic numbers can only weakly scatter the electrons, giving rise to a small shift in the transmitted electron wave phase [19]. Finally, polymers are found to be sensitive to electron irradiation, where incident electrons can break bonds, leading to structural changes [20]. These latter two points mean that, an advanced electron microscopic technique is required for the structural study of PVA.

Electron ptychography is a technique that uses 4D scanning transmission electron microscopy (STEM) dataset, where 2D convergent beam electron diffraction (CBED) patterns can be acquired at each 2D probe position in a raster scan [21]. High-angle annular dark field (HAADF) imaging generates an incoherent image using high-angle scattered electrons [22]. HAADF is highly sensitive to variations in the atomic number of atoms in the sample (Z-contrast images), and therefore, this technique is commonly used to identify materials with a higher Z in a matrix of material with a lower Z, causing heavier atoms to appear brighter in the resulting image [23]. As shown in Fig. 2, compared to HAADF STEM imaging, an extra fast pixelated detector is required to collect CBED patterns at a high speed at each probe pixel [24,25]. Moreover, HAADF can be recorded simultaneously because electron ptychography does not require lens aberration to form contrast [26,27]. Several previous studies have proved that ptychographic phase images retrieved from the 4D datasets can generate phase contrast to light atoms, where carbon, oxygen [28,29], and even lithium atoms [29] can be viewed in reconstructed images via Single-Side Band (SSB) or Wigner Distribution Deconvolution (WDD) methods [28]. Furthermore, STEM can reduce beam damage [30], especially for polymer samples [31,32], and electron ptychography uses dose with a higher efficiency, allowing a lower beam current, and thus, further reducing the beam damage to the samples [26,27].

The advantages of electron ptychography discussed above are helpful in overcoming the existing challenges for the microstructural study of PVA. In this work, we use electron ptychography to image PVA, and we expect the atomic-scale imaging of PVA can assist us in revealing the precise structure of the PVA crystal.

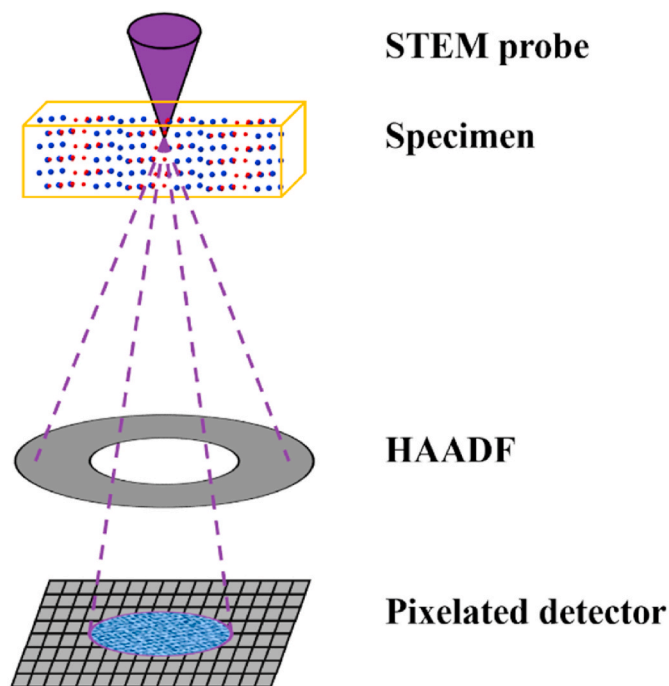


Fig. 2. Scheme of electron ptychography in STEM.

Two viewing directions are discussed in this microscopy work, namely the $[010]$ viewing direction and the $[\bar{1}10]$ viewing direction. Here, we take Bunn's model as an example to illustrate these two viewing directions and relevant d-spacings between planes, as shown in Fig. 3. As in Fig. 1, all oxygen sites in Fig. 3 represent a half-occupancy of oxygen atoms. In the $[010]$ viewing direction, the molecular axis is parallel to the viewing direction, and the carbon backbone zigzags as we move along the viewing direction. In the $[\bar{1}10]$ viewing direction, the molecular axis is parallel to the y axis, and lies at an oblique angle to the viewing direction, (shown in Fig. 3c). According to Bunn's model, the (100) spacing at 0.78 nm and (001) spacing at 0.55 nm can be detected in the $[010]$ viewing direction, and in the $[\bar{1}10]$ viewing direction, (001) spacing at 0.55 nm and (110) spacing at 0.24 nm should be found. In our work, these spacings are key features to identify PVA crystals when we study the experimental data.

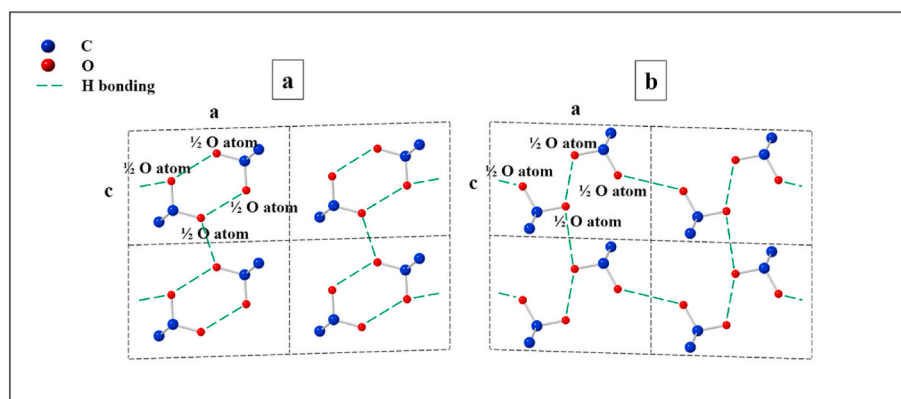


Fig. 1. Previous diffraction-derived PVA models viewed along the $[010]$ direction (along the molecular axis). Hydrogen bonding in the figure is indicative. (a) Bunn's model. (b) Sakurada's model.

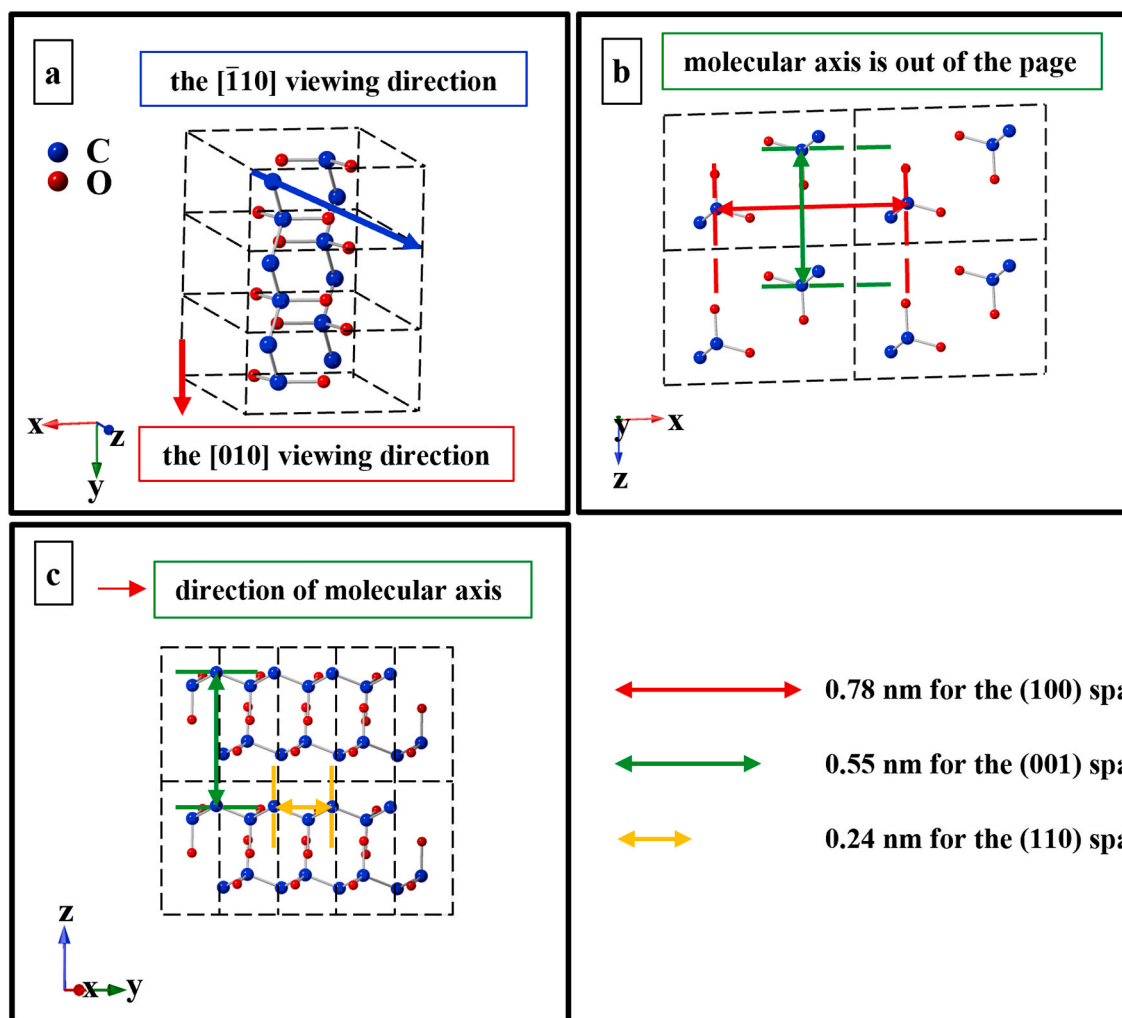


Fig. 3. Scheme of Bunn's model. (a) An oblique view of Bunn's model. (b) View along the $[010]$ viewing direction, which, for this monoclinic crystal structure, coincides with the molecular axis. (c) View along the $[\bar{1}10]$ viewing direction, the molecular axis is parallel to the y axis.

2. Experimental sections

2.1. XRD sample preparation and XRD data collection

PVA (99%, Mw 31,000–50,000, 98–99% hydrolysed, Aldrich) was firstly dissolved in deionised water at between 80 and 90 °C with 30 min continuous stirring to achieve a 10 wt% PVA solution. This PVA solution was dip-casted for 20 s onto Si substrates. Casted PVA thin-film samples were then freeze-thawed or annealed. The freeze-thawing process consists of three cycles, and each cycle contains 20-h freezing at -25 °C and 4-h thawing at room temperature. After three cycles, the freeze-thawed samples were air-dried overnight at room temperature. Annealing was carried out at different temperatures between 160 °C and 250 °C. Before annealing, thin-film PVA samples were air-dried overnight at room temperature. Then, samples were placed onto a hot plate. Referring to previous studies [18], the annealing time was decreased with the increase in temperature, where 160 °C for 20 min, 190 for 15 min, 220 for 10 min and 250 for 5 min. After annealing, the samples were cooled rapidly on a steel block.

XRD analysis was conducted VIA Rigaku Miniflex diffractometer with a Cu $K\alpha$ radiation at $\lambda = 0.154$ nm under 40 mA and 40 kV. The 2θ range is 10° – 60° , with a step size of 0.007° . XRD data were processed via X'Pert Highscore software.

2.2. Electron microscope sample preparation and HRTEM data collection

10 wt % PVA aqueous solution was dip-casted directly onto TEM grids (copper with lacey carbon films support, 400 mesh, Agar). TEM samples were then prepared using the annealing method at 250 °C introduced above.

Held by the single-tilt holder ($\pm 25^\circ$), the sample features and crystallinity were characterised by a high vacuum JEOL 3000F analytical TEM under 200 keV connected to a 4K Gatan Ultrascan filtered camera. HRTEM data were then processed using Gatan Digital Micrograph software.

2.3. 4D-STEM and its simultaneous HAADF data collection and reconstruction

An aberration-corrected JEOL ARM200F electron microscope operated at 200 kV was used for the electron microscopy study. The camera length for both images was 8 cm. Convergence angles were 14 mrad for the $[010]$ image and 22.5 mrad for the $[\bar{1}10]$ image. The probe currents were 57 pA for the $[010]$ image and 16 pA for the $[\bar{1}10]$ image. In the 4D STEM dataset recording, a focused STEM probe was used and the 2D CBED pattern at each probe position was recorded using a JEOL 4Dcanvas pixelated detector mounted on ARM200F. Through pixel binning by 4-fold by binning fast mode (dwell time is 133 μ s for each pixel), 4D datasets were recorded. The aberration-corrected ADF images

were recorded simultaneously using the JEOL ADF detector with the collection of 2D diffraction patterns. Data were processed and reconstructed by MATLAB scripts using Wigner distribution deconvolution method. Details of the electron ptychographic reconstructions can be found in some previous papers published by our group [26,28,33,34].

2.4. Model modification and image simulation

The whole PVA model modification process shown in Figs. 9 and 10 is achieved using MATLAB scripts.

4D-STEM simulations of the new model in [010] and $[\bar{1}10]$ direction is carried out using MULTTEM [35] and customised MATLAB scripts. A complete static lattice is simulated which is reasonable given that quantitative intensities are not required. The simulated 4D-STEM datasets are used for ptychography reconstruction and integration for virtual ADF images. An acceleration voltage of 200 kV is applied for the simulations as in experiments. Convergence angles used are 14 mrad for the [010] direction and 22.5 mrad for the $[\bar{1}10]$ direction. A perfect probe without aberrations is used in simulations. Simulated pixel size of scanning is 0.27 Å with 128×128 diffraction patterns (the [010] direction) and 0.13 Å with 175×175 diffraction patterns (the $[\bar{1}10]$ direction). The scanning coordinates are meanwhile collected. The simulated pixelated detector has 256×256 pixels with a pixel size of 1 mrad. Spot sizes of 1.25 Å and 0.65 Å are applied for the [010] direction and the $[\bar{1}10]$ direction, respectively. The sample thickness is set at 40 Å, and with the top surface of sample placed at the focal plane.

After simulation for 4D-STEM datasets, Poisson noise corresponding to electron dose is used to simulate a dose condition that is similar to experiments. The virtual ADF images are then integrated from collection angle higher than 72 mrad for both directions. Ptychography phase images are finally reconstructed using Wigner distribution deconvolution method, [21,23,28,33,36].

3. Results and discussion

3.1. XRD analysis

A thin-film PVA sample with a good degree of crystallinity is necessary for the electron microscopic study, and our work started with a study on increasing the crystallinity of solution-cast PVA. Inspired by previous findings, we applied freeze-thawing and annealing as methods to achieve a greater degree of crystallinity. X-ray diffraction (XRD) is utilised to test the effects of these two methods. As shown in Fig. 4, in the XRD trace (lowest line) confirmed unprocessed solution cast thin-film of PVA shows little or no crystallinity. In contrast, the freeze-thawed PVA sample starts to form more crystals as indicated by the small peak close to 20° 2θ . Furthermore, the annealed samples have the highest crystallinity among these three methods, and a higher annealing temperature contributes to a higher degree of crystallinity, ultimately showing multiple, sharp peaks in the XRD trace arising from the polymer crystals. XRD results here bring the overall crystal information of the PVA crystal, and the results accord with the previous studies [18]. Based on the XRD results, we decided to choose annealing at 250°C as the sample preparation method for the microscopic work.

3.2. Beam damage study on PVA

After excessive electron exposure of the PVA samples, evidence of beam damage can be seen. Fig. 5 shows the second scan of a PVA sample image after the first scan in this area, with a slight move of the sample. This move introduced some fresh material on the left side of the image that had not previously been exposed to the electron beam. The dose applied in this fresh area is 2.9×10^4 ($\text{e}^-/\text{Å}^2$). From the image, we can get clear patterns on the left, virgin, side, while the right side that had previously been exposed has reduced contrast. This image shows that on

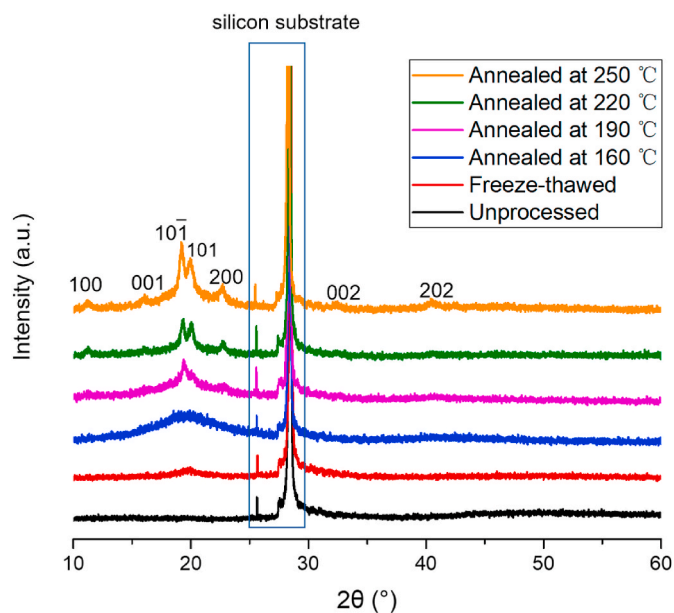


Fig. 4. XRD patterns of PVA thin-film samples including unprocessed one, freeze-thawed one and a series of samples after annealing at temperatures between 160°C and 250°C for 20min.

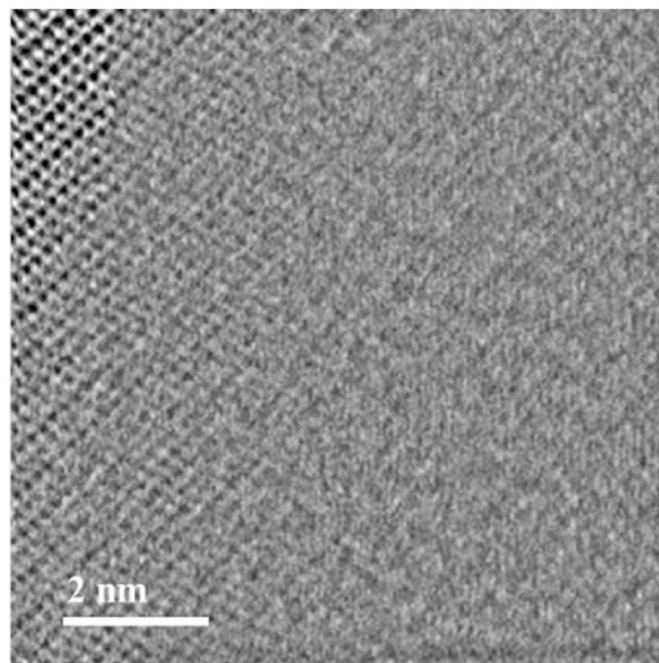


Fig. 5. Second WDD acquisition with a slight sample move on the PVA sample.

the PVA sample, the process of damage is likely to be amorphization. This result tells us that a limited dose is important for the electron ptychographic study, and normally, the first-round acquisition is most likely to bring the clearest image of the area. This is also important because it means that the crystallinity we are seeing is not due to beam effects.

3.3. Electron microscopic imaging of PVA

Turning to the microscopic work, prior to the electron ptychographic study, we used HRTEM to get the basic crystal information of PVA and further confirm the effects of annealing. As a result of the annealing, we

were able to image a single-crystal region of sample, and clear fringes can be observed in the HRTEM image (in Fig. 6a). Calculating the d-spacings via line profiles from 10 different measurements, a 0.40 ± 0.01 nm d-spacing was measured from the image, and its FFT image in Fig. 6d also shows some other d-spacings at $0.45 (\pm 0.02)$ nm, $0.26 (\pm 0.01)$ nm, $0.22 (\pm 0.01)$ nm and so on. To understand the information, we simulated the single-crystal electron diffraction pattern of Bunn's PVA model (in Fig. 6g). In summary, d-spacings above can be associated with the (200), (002), (101) and (202) planes respectively using the FFT pattern. Taking two typical spacings as an example, shown in Fig. 6h the 0.40 ± 0.02 nm and 0.26 ± 0.03 nm acquired from electron microscopic images accord with the d-spacings of the (200) and (002) planes of PVA from Bunn's model.

Following the HRTEM, the same crystal of the PVA sample was also imaged via electron ptychography and its simultaneous HAADF-STEM image. Collection angles for HAADF images are from 72 to 271 mrad. The dose here is 6.5×10^4 ($e^-/\text{\AA}^2$), and no severe beam damage was found during the acquisition. The reconstructed WDD-phase image and the HAADF image are shown in Figs. 6c and b, respectively. The d-spacings acquired from these two images are the same as the ones obtained from the HRTEM image, and the d-spacings are marked in Figs. 6c and b and their FFT images of Figs. 6f and e. Comparing the HAADF and the electron ptychographic image, Fig. 6c shows much more detail than Fig. 6b, and thus, electron ptychography brings more information on the structure, and the image shows how the light atoms order in the material in the [010] viewing direction.

Information from another viewing direction can facilitate under-

standing of the structure. As shown in Fig. 7, another series of microscopic images are acquired via HAADF-STEM (Fig. 7a) and electron ptychography (Fig. 7b). Collection angles for HAADF images are from 72 to 271 mrad. The dose here is 7.9×10^4 ($e^-/\text{\AA}^2$), and no severe beam damage was found during the acquisition. From the images, two d-spacings at 0.55 ± 0.03 nm and 0.23 ± 0.03 nm can be found. As shown in Fig. 7e, comparing the FFT of the electron ptychographic image (Fig. 7c) and simulated single-crystal electron diffraction pattern (Fig. 7d), 0.55 nm and 0.23 nm correspond to the (001) and (110) d-spacings of PVA, and the viewing direction that we acquired information from is $[\bar{1} 10]$. It should be noted that the (001) d-spacing was not observed in the [010] viewing direction, and the reason for this will be discussed later.

As for the crystallographic information, all d-spacings acquired from XRD and electron ptychography are presented in Table 1. As shown in Fig. 6g and Table 1, although key spacings found in electron microscopic images are consistent with the XRD and simulated results, there are still some differences between them. Firstly, the d-spacings of (110) and (111) planes are not clearly found in the XRD data, which can be attributed to the low intensity and overlapping of the signals of the above-mentioned planes to the (202) plane, as their d-spacings and hence 2θ angle detected in XRD are very close. Another important discrepancy is the absence in the FFT of the [010] electron microscopic image of spots corresponding to (100) (purple square in Fig. 6g) and (001) (grey square in Fig. 6g) planes, even though diffraction spots for these planes are observed in XRD, and are reproduced in the electron diffraction simulation, in this case from Bunn's model. In the simulated

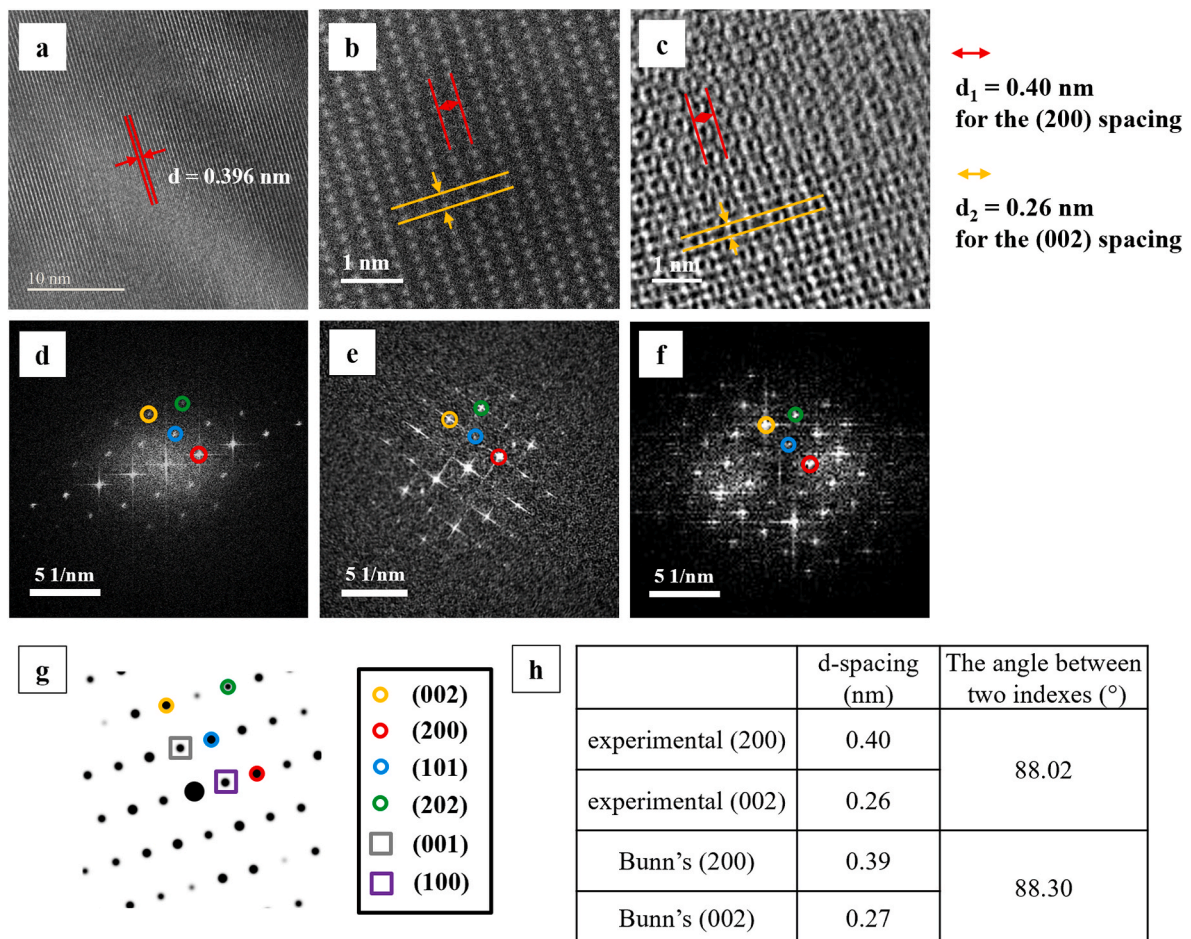


Fig. 6. Electron microscopic and simulated images of PVA orientated in the [010] viewing direction. (a) HRTEM image. (b) HAADF-STEM image. (c) Simultaneous electron ptychography WDD phase image. (d) FFT of (a). (e) FFT of (b). (f) FFT of (c). (g) Simulated single-crystal electron diffraction pattern of Bunn's model. (h) Comparison between electron ptychographic data and Bunn's model.

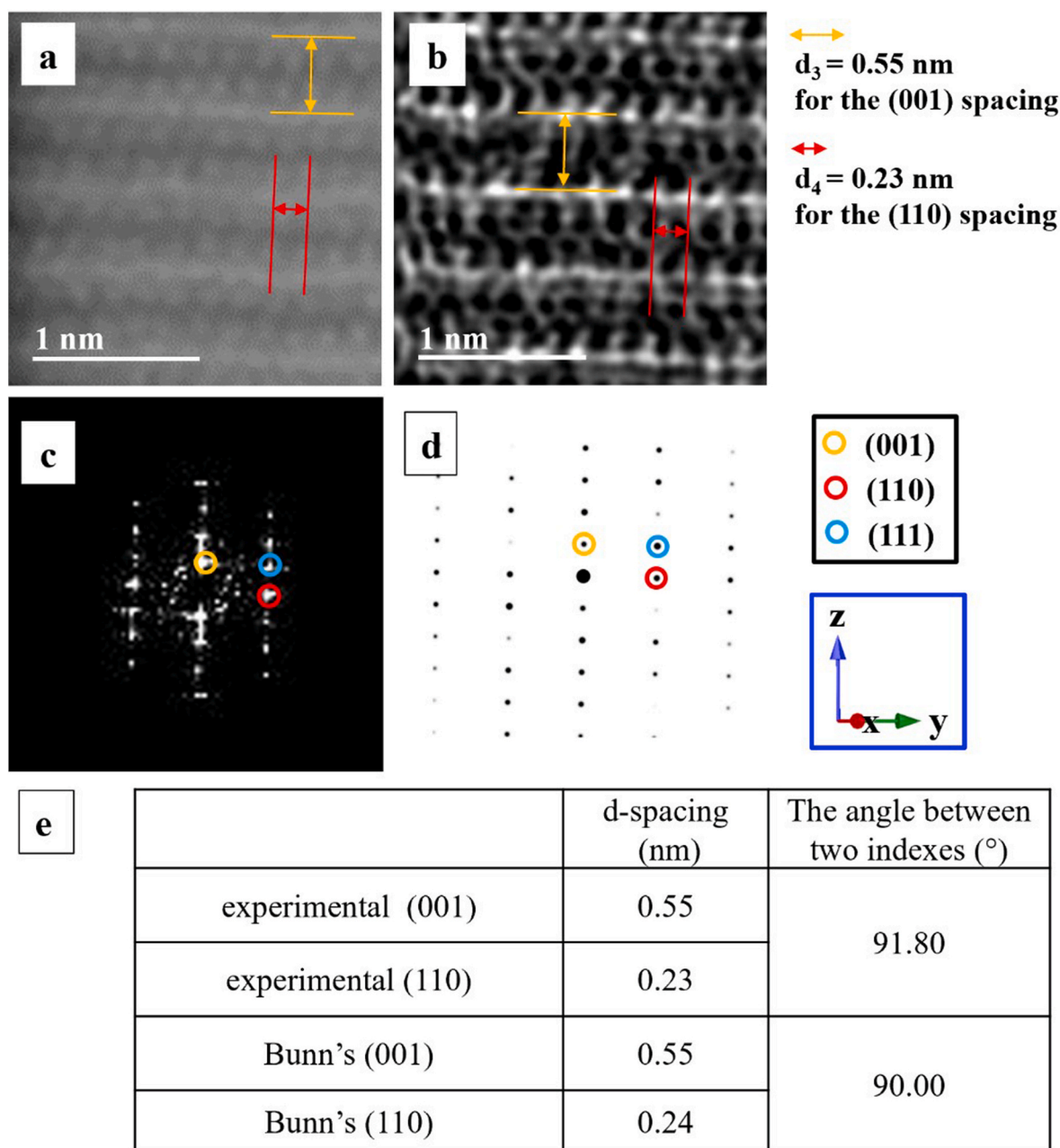


Fig. 7. Electron microscopic images of PVA orientated in the $[\bar{1}10]$ viewing direction. (a) HAADF-STEM image. (b) Simultaneous electron ptychography WDD phase image. (c) FFT of b. (d) Simulated single-crystal electron diffraction pattern of Bunn's model. (e) Comparison between experimental data and Bunn's model.

electron diffraction pattern, the (100) and (001) signals are relatively weak, which indicates the periodicities of (100) and (001) are weaker than those of (200) and (002). From Bunn's model, we expect to see the (100) and (001) reflexions as the intermediate molecules between these planes do not lie at precisely the half-way point nor in the same orientation. Therefore, the disappearance of (100) and (001) spacings in the microscopic images cannot be accounted for by a structure consisting simply of either the Bunn or the Sakurada model. In particular, the experimental images suggest a structure in which half the molecules lie at the midpoints of these planes rendering them forbidden reflections, and this can eliminate the (100) and (001) signals [37,38]. At this stage, some different description of the structure is necessary to interpret the experimental data. The model modification process will be introduced below, and then, the disappearance of (100) and (001) spacings will be further discussed with the aid of a new description of the PVA structure.

A comparison between the electron ptychographic image and the

previous models can be helpful to further investigate the discrepancy. As shown in Fig. 7, when superposing each of the two extant models on the electron ptychography image, no matter whether Bunn's model (in Fig. 8a) or Sakurada's model (in Fig. 8b) is used, only half of the spots in the electron ptychographic image match each of the two previous models. Considering that (100) and (001) are not present in the FFT of the [010] images, symmetrising the PVA model could be helpful to fit the experimental results. Additionally, the presence of elongated features (which may indicate oxygen atoms stacked along this projection) between the bright spots (which may indicate carbons stacked along this projection) suggests that the real PVA crystal allows more possible oxygen positions than either of the previously models would, individually, suggest. As differences can be found in both microscopic images and FFT results, further modifications to our understanding of the PVA crystal structure are required.

Similar to the images taken from the [010] viewing direction, an

Table 1

Summary of d-spacings acquired from XRD, HAADF and electron ptychography.

| XRD acquired | | HAADF and electron ptychography acquired | | |
|-----------------|------------------|--|---------------------------------|---|
| d-spacings (nm) | plane | d-spacings (nm) | Plane | in which viewing direction the d-spacing was acquired |
| 0.79 | (1 0 0) | 0.40 | (2 0 0) | (0 1 0) |
| 0.55 | (0 0 1) | 0.26 | (0 0 2) | |
| 0.46 | (1 0 1) | 0.45 | (1 0 1) and/or (1 0 $\bar{1}$) | |
| 0.45 | (1 0 $\bar{1}$) | 0.22 | (2 0 2) | |
| 0.39 | (2 0 0) | 0.55 | (0 0 1) | ($\bar{1}$ 1 0) |
| 0.27 | (0 0 2) | 0.23 | (1 1 0) | |
| 0.22 | (2 0 2) | 0.21 | (1 1 1) | |

electron ptychographic image in the $[\bar{1} 10]$ direction also brings more information on PVA than HAADF-STEM. To figure out how the light atoms order in the viewing direction, we also superimposed previous models onto the electron ptychographic image (shown in Fig. 9). All oxygen sites in Fig. 9 represent half the occupancy of oxygen atoms. We find that the shapes of the original models look close to the image in the $[\bar{1} 10]$ viewing direction, but some differences are obvious. For instance, in the image, there is a mid layer between two intense layers, but in Bunn's model (in Fig. 9a), all layers (parallel carbon backbones with side oxygens) should have the same electron density, and hence the same contrast in the electron microscopic image. There is a certain amount of non-periodic structure observable as one passes along the chain axis. Therefore, a modification of the PVA crystal model based on images taken on $[010]$ and $[\bar{1} 10]$ directions are required to fit the image well.

3.4. PVA model modification

Given the observed absence of spots associated with the (100) and (001) in the FFT of the microscopy images that would not be expected from the XRD-derived models, we propose here a new description of the PVA structure which takes into account the possibility that the backbone of the molecule may rotate and shift, allowing for intermolecular H-bonding in many different directions. This may not be the thermodynamic minimum energy structure, but as the crystals form, the more disordered structure may be locked in due to the crystallization kinetics. In this paper, we have not modelled the energetics of the local backbone twisting that would be required for such a rotation or a shift, but rather consider the consistency of this model with the observed imaging.

The whole model modification process as observed in the $[010]$ viewing direction is schematically illustrated in Fig. 10. Based initially on Sakurada's model, the model modification starts by rotating each molecule around the $[010]$ (molecular) axis in 90 steps and then superimposing them on one another along the y (molecular) axis. This step reasonably gives explorable configurations of hydrogen bonding, appealing to the difference between Bunn and Sakurada's models. No account is made here of the connectivity of C-atoms between one rotation and the next, and the positions shown are only approximate. As shown in Fig. 10a, "star" groups are produced after step 1. Note that the carbon (and oxygen) atoms shown in this viewing direction show the possible locations of carbon (and oxygen), they do not represent the position of atoms in every unit cell repeat. From the $[001]$ viewing direction shown in Fig. 10b, the superimposed model can be understood better. Herein, layer A refers to the original form (it will be marked as 0° in the following), and layer B was generated by rotating 90° clockwise around the $[010]$ (molecular) axis from A (it will be marked as 90° in the following). In the same manner, layer C (180° rotated clockwise from A) and layer D (270° rotated clockwise from A) can be also developed. After superimposing 0° (A), 90° (B), 180° (C) and 270° (D) along the molecular axis, two "stars" can be viewed from the $[010]$ viewing direction in

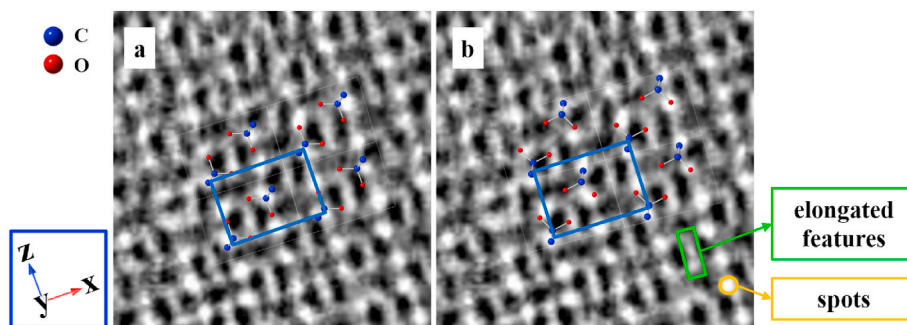


Fig. 8. Enlarged WDD phase image superposed with previous models orientated in the $[010]$ viewing direction. (a) WDD phase image with Bunn's model. (b) WDD phase image with Sakurada's model.

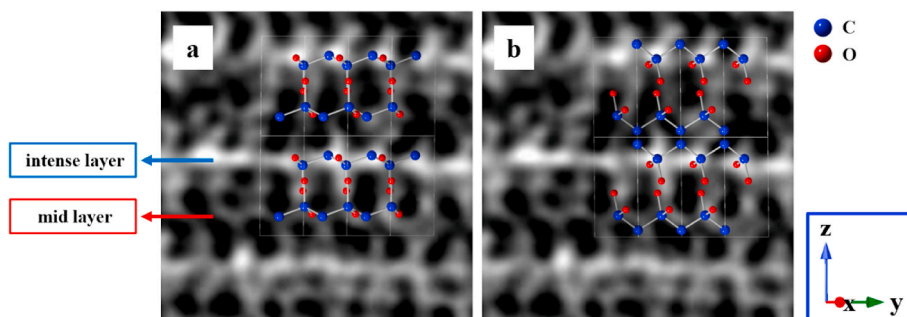


Fig. 9. Enlarged WDD phase image superposed with previous model orientated in the $[\bar{1} 10]$ viewing direction. (a) WDD phase image with Bunn's model. (b) WDD phase image with Sakurada's model.

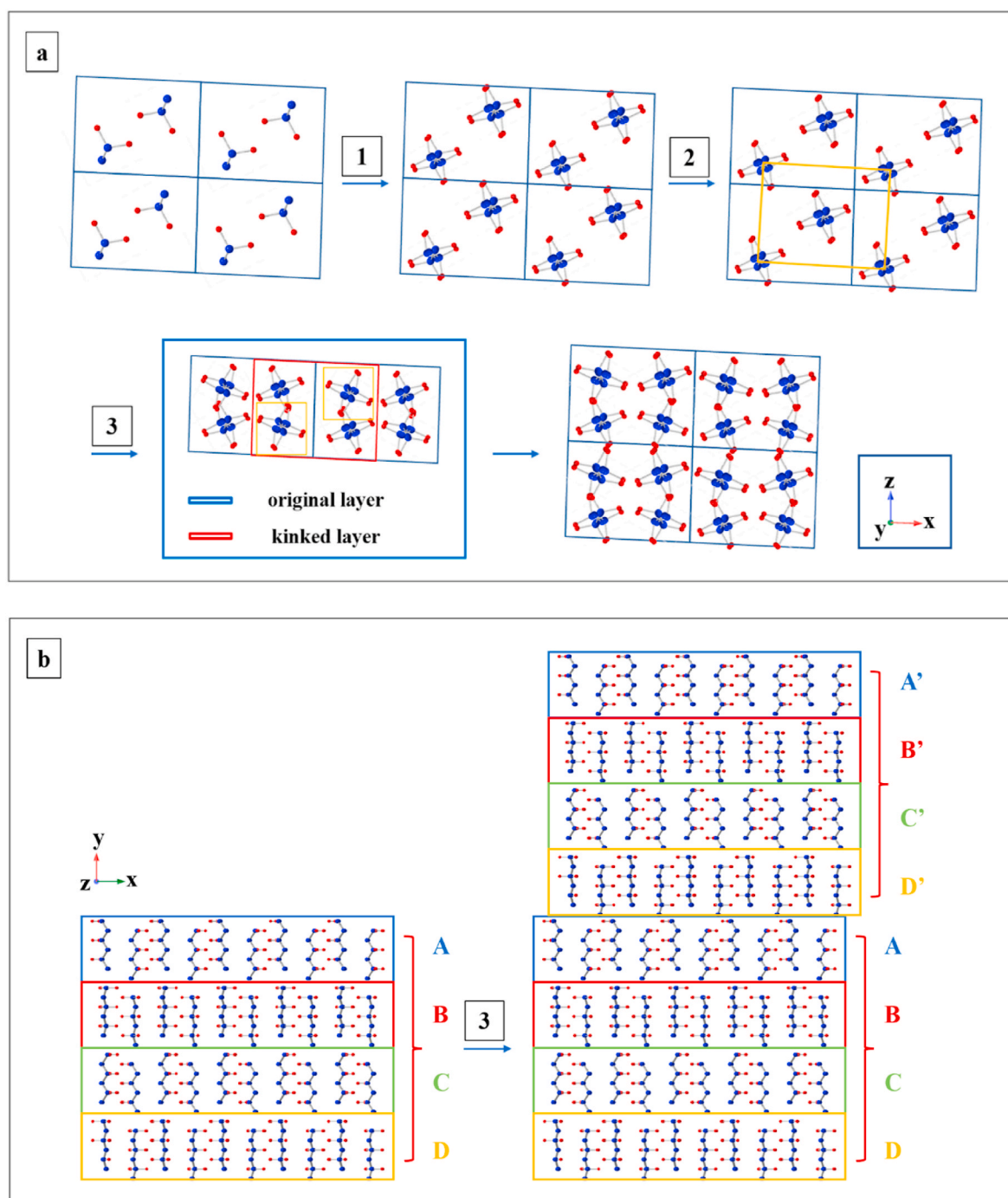


Fig. 10. Schematic illustration of the model modification process as observed in the [010] viewing direction (all oxygen sites represent half the occupancy of oxygen atoms). (a) The whole process of PVA model modification includes three steps. Note that the carbon (and oxygen) atoms shown in this viewing direction show the possible locations of carbon (and oxygen) they do not represent the position of atoms in every unit cell repeat. However, all such locations will be represented in the projection of many unit cells along this axis. (b) Explanation of the third step, viewing from the [001] direction.

a PVA crystal unit cell. The rotation angle in this step is just close to the PVA unit cell parameter β (91.7° in Bunn's model and 87.0° in Sakurada's model), which means rotating does not change the crystal structure but just forms variations of the original formation.

After that, step 2 symmetrising means to move the central star-shape atoms (to the centre of the orange parallelogram marked in Fig. 10a). The motivation here is to match the experimental data better, and the symmetry would eliminate signals from (100) and (001) planes in the microscopic images by making the associated diffraction reflections forbidden [37,38].

Next, a shift of the whole package of ABCD is operated in Procedure 3 (in Fig. 10b) to half a unit cell along the x axis, then we rotate the shifted two stars 45° clockwise, such that adjacent oxygens face one another to form intermolecular hydrogen bonds. This is done to achieve the spacing of intensities observed in the experimental images. This shift could represent a 'kink' in the chain for example, and once again it represents the possible occupancy of spaces, which when viewed in projection through many unit cells in the microscopy image, will appear as overlapping locations. To distinguish these from the original ABCD layers, here we call the shifted layers A'B'C'D'. The shifted and rotated unit cell

is shown in Fig. 10b after Procedure 3. From the [010] viewing direction shown in Fig. 10a, four “stars” including two “stars” marked in orange squares from the new layers can be viewed in the middle PVA unit cell. The modification of PVA crystal is now completed, and the whole process is due to the flexibility of polymer backbones and the influence of hydrogen bonding, and this new structure can make the PVA crystal that forms.

In this part, we need to put some more additional notes. First, it was clear from the electron ptychographic image taken in the [010] viewing direction, including the lines between bright spots, the positions of oxygens are flexible, the new model represents the average positions of the atoms in the PVA crystals. Secondly, the 8-layer structure shown in Fig. 11b can be periodic like ABCDA'B'C'D' or more likely random like ACDBB'A'C'D', AACDB'C'C'D' etc., in practice.

3.5. Image simulation

The multislice method [39] enables us to simulate STEM and electron ptychographic images of structural models, and here we use the multislice method to simulate the images based on our new PVA model. Fig. 11 shows the experimental data, the new crystal model, and the simulated images of the PVA new model as observed in the [010] viewing direction. Simulation results have mostly the same spacings and configurations showing good agreement with the experimental data, where HAADF images show the orderings of carbon backbones, while electron ptychographic images provide additional information about oxygen positions. This supports our approach to modify the PVA model.

As for the $[\bar{1}10]$ viewing direction, after the series of model modification processes, d-spacings are the same in the experimental and simulated results. As shown in Fig. 12, electron ptychography reasonably closely reproduces the results, although the precise details in the HAADF images are not precisely reproduced. The new model still works

on this direction as the symmetry and the periodicity are the same in both sides, but the differences in the details likely arise from the high randomness of the oxygen atom's locations, depending on their local environment. Future studies on the PVA microstructure can further tune some details.

As the new model is supported by simulation data along both experimentally determined viewing directions, we can now use the model to illustrate the remaining question as to why the (001) and (100) disappeared from the FFT images viewed from the [010] direction. To answer this question, the difference between XRD and FFT images should firstly be discussed. The XRD intensity arises from the overall information of all the local interplanar spacings in the structure. In contrast, the microscopic imaging gives the average positions of the atoms projected through the whole thickness of the image (depth of focus).

Here, Fig. 13 is utilised to explain this further. With each of the individual models (Bunn's and Sakurada's), as indicated by green arrows in Fig. 13a, and blue arrows in Fig. 13b, in some cases, the distances between the backbones are different. Furthermore, in all cases, the positions of the oxygen atoms with respect to the backbone are different when considering the nearest repeat distances between the backbones perpendicular to the relevant planes. So locally, driven by the rotation of backbones and the randomness of the hydrogen bonding directions, the (001) and (100) d-spacings can lead to diffraction because the other molecules are not exactly at these plane midpoints, and the intensities can be captured by XRD. If the chain can randomly reorientate along the chain axis as we suggest in the PVA model modification section, the structure can move between Bunn-like and Sakurada-like models. Therefore, the projected average atomic positions will be the average of Bunn's and Sakurada's models. With the averaging, the projected atomic positions on average are more symmetric, and hence, the (100) and (001) d-spacings disappear from the FFT.

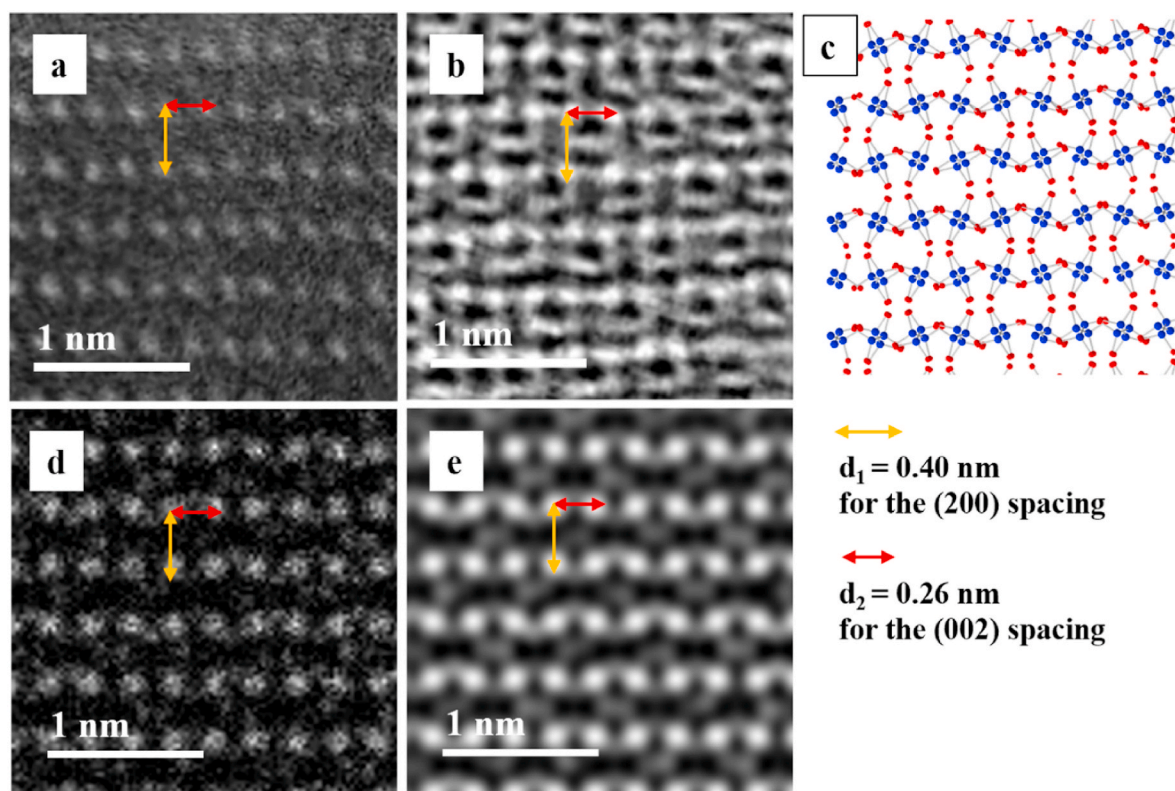


Fig. 11. Experimental and simulated images of PVA in the [010] viewing direction. (a) Experimental HAADF-STEM image. (b) Experimental electron ptychography WDD phase image. (c) The modified PVA structure by the method elaborated in Fig. 10 (all oxygen sites represent half the occupancy of oxygen atoms). (d) Simulated flat HAADF image. (e) Simulated electron ptychographic WDD-phase image.

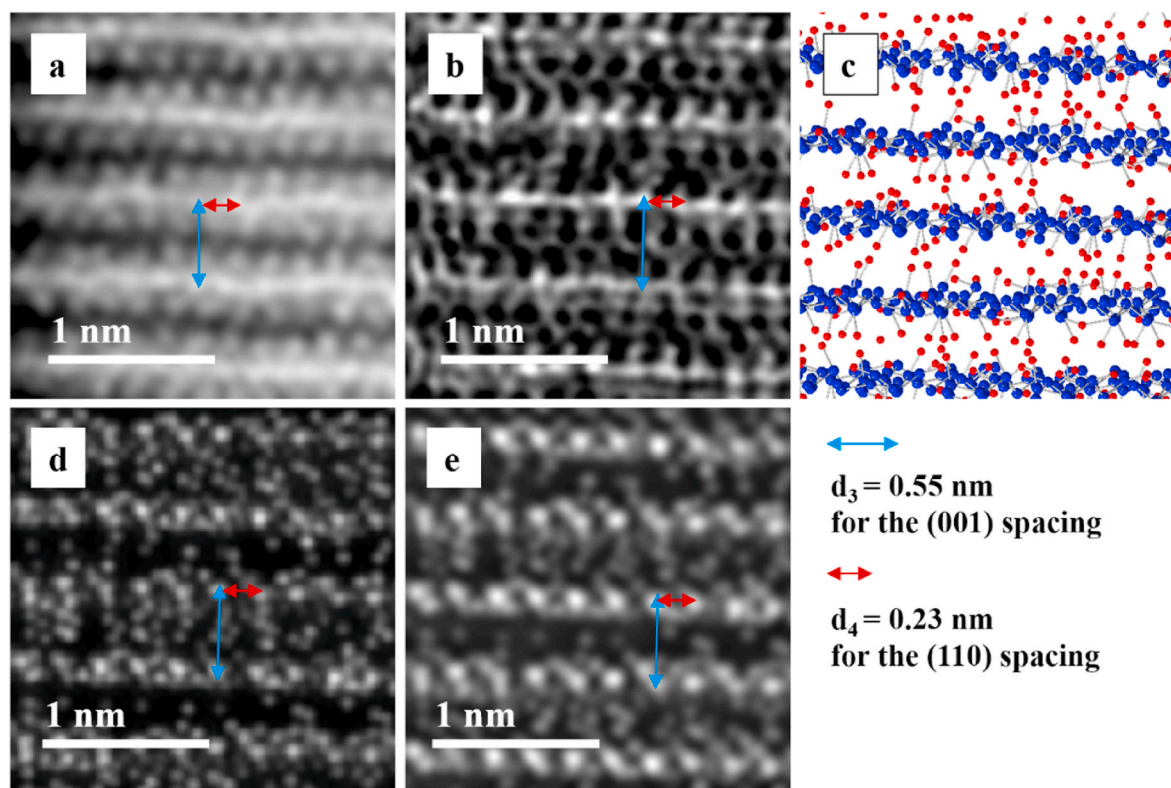


Fig. 12. Experimental and simulated images of PVA in the $[\bar{1}10]$ viewing direction. (a) Experimental HAADF image. (b) Experimental electron ptychography WDD phase image. (c) The modified PVA structure by the method elaborated in Fig. 10 (all oxygen sites represent half the occupancy of oxygen atoms). (d) Simulated flat HAADF image. (e) Simulated electron ptychographic WDD-phase image.

This example illustrates an important difference between a diffraction pattern and the FFT of a projected image in the case when there is randomness in the structure. The diffraction pattern reflects the average of the periodicity and symmetry of the local interactions, whereas the FFT of the projected image reflects the periodicity of the average positions of the atoms. Thus, the direct imaging of the crystal structure can provide direct evidence for more disorder in the crystal structure than can be ascertained from diffraction experiments alone.

4. Conclusions

In this work, we applied an advanced electron microscopic technique, electron ptychography, to image a challenging material, PVA, for which two alternative crystal structures have been mooted. The precondition to getting informative microscopic images is to have a highly crystallised PVA sample. Inspired by previous studies on PVA, we first used freeze-thawing and annealing methods for a higher crystallinity. As suggested by XRD results, annealing has the best effect, and the increase in annealing temperature further facilitates the crystallization of PVA. After that, HRTEM was operated for a basic study on PVA crystal prior to electron ptychography. Typical d-spacings of PVA at 0.40 nm for the (200) and 0.26 nm for the (002) plane of PVA were acquired. These d-spacings accord with the XRD data and the simulated results based on an old PVA model.

Electron ptychographic data with the simultaneous HAADF-STEM results were then acquired. Electron ptychographic data were reconstructed by SSB and WDD methods. Firstly, we understand the mechanism of beam damage of PVA is amorphization, and the crystal information we acquired is not due to beam effects. In the $[010]$ viewing direction, the same d-spacings got from HRTEM are detected in both images, but the spacings for the (100) and (001) planes are still missing. By comparison, electron ptychography brings more information than

HAADF-STEM, and the reconstructed ptychographic image shows how the light atoms order in the PVA. The ptychographic image shows some agreements with previous models, but deviations from previous models derived from X-ray diffraction are also observed.

Besides $[010]$, we also acquired images from the $[\bar{1}10]$ viewing direction. Two d-spacings at 0.55 nm and 0.23 nm can be found, and the simulated single-crystal electron diffraction pattern supports that they are the spacings for the (001) and (110) planes of PVA. Similar to the $[010]$ direction, electron ptychography also brings a clearer and more informative image than HAADF-STEM. However, both similarities and discrepancies are also found in the direction between the old models and the experimental results. Therefore, we utilised information from images taken on $[010]$ and $[\bar{1}10]$ projections to tune the PVA crystal model.

Without changing unit cell dimensions, the model modification process is composed of rotating, symmetrising and shifting. Finally, a multilayer PVA crystal model is constructed. The modification process is driven by the flexibility of polymer backbones and the randomness of hydrogen bonding directions. The symmetries of the new PVA model viewed from both directions are the same as their experimental images.

To further interpret the data, we then did image simulations on the new model. The multislice simulation results essentially accord with the experimental data, which supports our hypothesis to modify the model. Finally, the extinction of the (100) and (001) spacings in the $[010]$ viewing direction can be attributed to symmetry of the new model, where the projected average atomic positions can be the average of Bunn's and Sakurada's models. As the FFT of the projected image reflects the periodicity of the average positions of the atoms, the (100) and (001) d-spacings disappear from the FFT. However, XRD reflects the average of the periodicity and symmetry of the local interactions. The rotation of backbones and the randomness of the hydrogen bonding directions give rise to diffractions of the (001) and (100) d-spacings, and

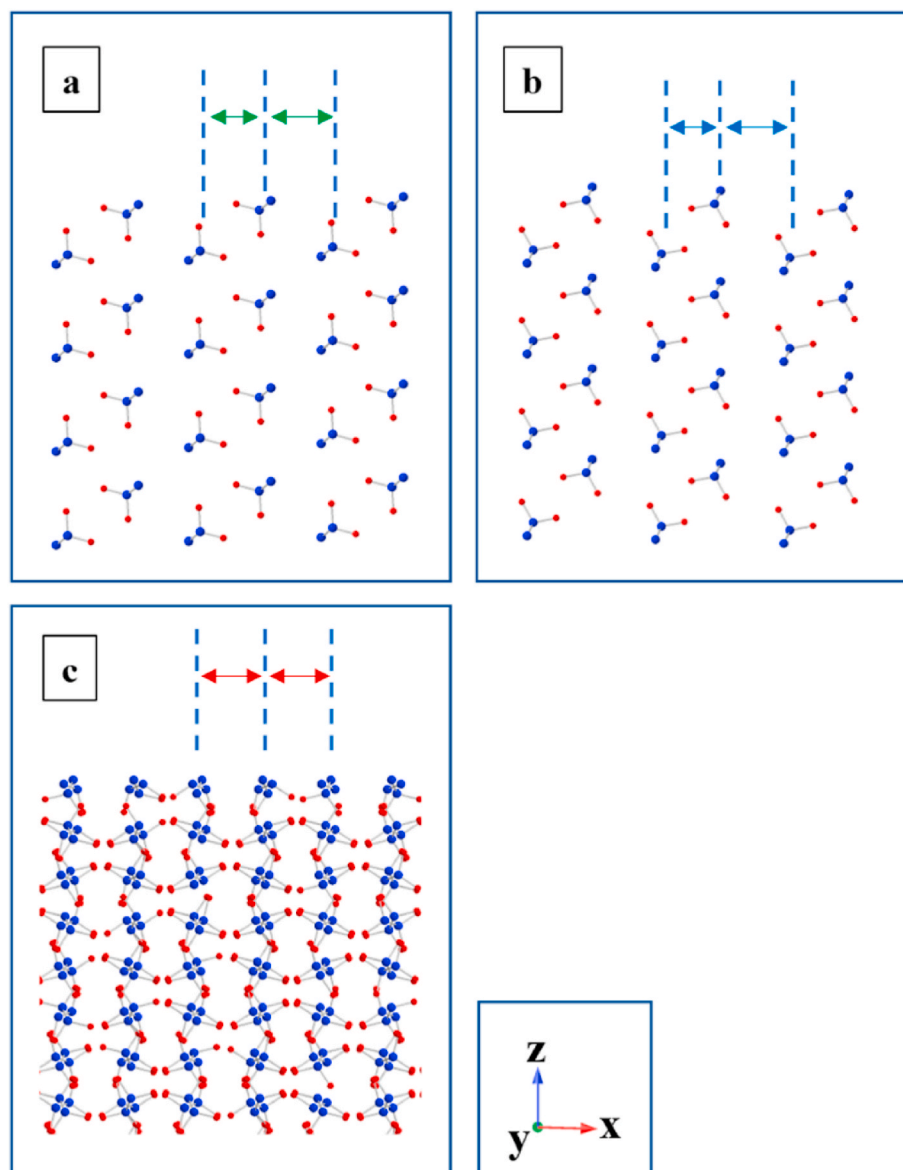


Fig. 13. PVA model models viewed from the [010] direction (all oxygen sites represent half the occupancy of oxygen atoms). (a) Bunn's model. (b) Sakurada's model. (c) The modified PVA structure by the method elaborated in Fig. 10.

their intensities can be captured by XRD.

In summary, by using electron ptychography, we managed to image the PVA crystal, which has not previously been achieved by any conventional methods. And with the aid of model modification and image simulation, the results bring us a new and deeper understanding of the PVA crystal structure. This suggests that the molecular configurations locked into the crystal are far more variable than suggested by the previous models. This can be achieved as there are multiple possible inter- and intramolecular hydrogen bonding directions depending on the nearest neighbour oxygen positions. This methodology can be expanded to other polymeric systems for better microstructural insights.

CRediT authorship contribution statement

Botao Hao: Conceptualization, Investigation, Writing – original draft. **Zhiyuan Ding:** Formal analysis. **Xudong Tao:** Investigation. **Peter D. Nellist:** Supervision, Writing – review & editing. **Hazel E. Assender:** Supervision, Writing – review & editing.

Declaration of competing interest

The authors declare that they have no known competing financial interests or personal relationships that could have appeared to influence the work reported in this paper.

Data availability

Data will be made available on request.

Acknowledgements

The authors acknowledge use of characterisation facilities within the David Cockayne Centre for Electron Microscopy, Department of Materials, University of Oxford and in particular the EPSRC (EP/K040375/1 “South of England Analytical Electron Microscope”) and additional instrument provision from the Henry Royce Institute (Grant reference EP/R010145/1). Technical support is also gratefully acknowledged from Richard Turner, Dr Weixin Song, Dr Ali Mostaed and Dr Xiaonan Luo from Department of Materials, University of Oxford.

References

- [1] D. Wong, J. Parasrampur, Polyvinyl alcohol, in: *Analytical Profiles of Drug Substances and Excipients*, Academic press, 1996, pp. 397–441, 24.
- [2] R. Nagarkar, J. Patel, Polyvinyl alcohol: a comprehensive study, *Acta Scientific Pharmaceutical Sciences* 3 (4) (2019) 34–44.
- [3] M.I. Baker, S.P. Walsh, Z. Schwartz, B.D. Boyan, A review of polyvinyl alcohol and its uses in cartilage and orthopedic applications, *J. Biomed. Mater. Res. B Appl. Biomater.* 100 (5) (2012) 1451–1457.
- [4] S. Muppalaneni, H. Omidian, Polyvinyl alcohol in medicine and pharmacy: a perspective, *J. Dev. Drugs* 2 (3) (2013) 1–5.
- [5] S. Saha, M.K. Mishra, C.M. Reddy, G.R. Desiraju, From molecules to interactions to crystal engineering: mechanical properties of organic solids, *Accounts Chem. Res.* 51 (11) (2018) 2957–2967.
- [6] D. Mileva, D. Tranchida, M. Gahleitner, Designing polymer crystallinity: an industrial perspective, *Polymer Crystallization* 1 (2) (2018), e10009.
- [7] J.E. Mark (Ed.), *Physical Properties of Polymers Handbook*, vol. 1076, Springer, New York, 2007, p. 825.
- [8] C.W. Bunn, Crystal structure of polyvinyl alcohol, *Nature* 161 (4102) (1948) 929–930.
- [9] I. Sakurada, K. Fuchino, N. Okada, Crystal structure of polyvinyl alcohol, *Bull. Inst. Chem. Res. Kyoto Univ.* 23 (1950) 78–79, 1950.
- [10] H. Li, W. Zhang, W. Xu, X. Zhang, Hydrogen bonding governs the elastic properties of poly (vinyl alcohol) in water: single-molecule force spectroscopic studies of PVA by AFM, *Macromolecules* 33 (2) (2000) 465–469.
- [11] B. Briscoe, P. Luckham, S. Zhu, The effects of hydrogen bonding upon the viscosity of aqueous poly (vinyl alcohol) solutions, *Polymer* 41 (10) (2000) 3851–3860.
- [12] L. Dai, L. Ying, Infrared spectroscopic investigation of hydrogen bonding in EVOH containing PVA fibers, *Macromol. Mater. Eng.* 287 (8) (2002) 509–514.
- [13] H.E. Assender, A.H. Windle, Crystallinity in poly (vinyl alcohol) 2. Computer modelling of crystal structure over a range of tacticities, *Polymer* 39 (18) (1998) 4303–4312.
- [14] B. Briscoe, P. Luckham, S. Zhu, The effects of hydrogen bonding upon the viscosity of aqueous poly (vinyl alcohol) solutions, *Polymer* 41 (10) (2000) 3851–3860.
- [15] C.M. Hassan, N.A. Peppas, Structure and morphology of freeze/thawed PVA hydrogels, *Macromolecules* 33 (7) (2000) 2472–2479.
- [16] B.S. Chee, G.G. de Lima, D.M. Devine, M.J. Nugent, Investigation of the effects of orientation on freeze/thawed Polyvinyl alcohol hydrogel properties, *Mater. Today Commun.* 17 (2018) 82–93.
- [17] H. Adelnia, R. Ensandoost, S.S. Moonshi, J.N. Gavvani, E.I. Vasafi, H.T. Ta, Freeze/thawed polyvinyl alcohol hydrogels: present, past and future, *Eur. Polym. J.* (2021), 110974.
- [18] H.E. Assender, A.H. Windle, Crystallinity in poly (vinyl alcohol). 1. An X-ray diffraction study of atactic PVOH, *Polymer* 39 (18) (1998) 4295–4302.
- [19] M.R. McCartney, P. Kruit, A.H. Buist, M.R. Scheinfein, Differential phase contrast in TEM, *Ultramicroscopy* 65 (3–4) (1996) 179–186.
- [20] L. Sawyer, D.T. Grubb, G.F. Meyers, *Polymer Microscopy*, Springer Science & Business Media, 2008.
- [21] P.D. Nellist, B.C. McCallum, J.M. Rodenburg, Resolution beyond the 'information limit' in transmission electron microscopy, *Nature* 374 (6523) (1995) 630–632.
- [22] D.E. Jesson, S.J. Pennycook, Incoherent imaging of crystals using thermally scattered electrons, *Proc. Roy. Soc. Lond. Math. Phys. Sci.* 449 (1995) 273–293, 1936.
- [23] P.D. Nellist, S.J. Pennycook, The principles and interpretation of annular dark-field Z-contrast imaging, *Adv. Imag. Electron. Phys.* 113 (2000) 147–203. Elsevier.
- [24] H. Yang, R.N. Rutte, L. Jones, M. Simson, R. Sagawa, H. Ryll, M. Huth, T. J. Pennycook, M.L.H. Green, H. Soltau, Y. Kondo, B.G. Davis, P.D. Nellist, Simultaneous atomic-resolution electron ptychography and Z-contrast imaging of light and heavy elements in complex nanostructures, *Nat. Commun.* 7 (1) (2016), 12532.
- [25] H. Ryll, M. Simson, R. Hartmann, P. Holl, M. Huth, S. Ihle, Y. Kondo, P. Kotula, A. Liebel, K. Müller-Caspary, A. Rosenauer, R. Sagawa, J. Schmidt, H. Soltau, L. Strüder, A pnCCD-based, fast direct single electron imaging camera for TEM and STEM, *J. Instrum.* 11 (2016), P04006, 04.
- [26] T.J. Pennycook, A.R. Lupini, H. Yang, M.F. Murfitt, L. Jones, P.D. Nellist, Efficient phase contrast imaging in STEM using a pixelated detector. Part 1: experimental demonstration at atomic resolution, *Ultramicroscopy* 151 (2015) 160–167.
- [27] H. Yang, T.J. Pennycook, P.D. Nellist, Efficient phase contrast imaging in STEM using a pixelated detector. Part II: optimisation of imaging conditions, *Ultramicroscopy* 151 (2015) 232–239.
- [28] H. Yang, I. MacLaren, L. Jones, G.T. Martinez, M. Simson, M. Huth, H. Ryll, H. Soltau, R. Sagawa, Y. Kondo, C. Ophus, P. Ercius, L. Jin, A. Kovács, P.D. Nellist, Electron ptychographic phase imaging of light elements in crystalline materials using Wigner distribution deconvolution, *Ultramicroscopy* 180 (2017) 173–179.
- [29] W. Song, M.A. Pérez-Osorio, J.J. Marie, E. Liberti, X. Luo, C. O'Leary, R.A. House, P.G. Bruce, P.D. Nellist, Direct imaging of oxygen shifts associated with the oxygen redox of Li-rich layered oxides, *Joule* 6 (5) (2022) 1049–1065.
- [30] M. Ilett, R. Brydson, A. Brown, N. Hondow, Cryo-analytical STEM of frozen, aqueous dispersions of nanoparticles, *Micron* 120 (2019) 35–42.
- [31] M.R. Libera, R.F. Egerton, Advances in the transmission electron microscopy of polymers, *Polym. Rev.* 50 (3) (2010) 321–339.
- [32] R.F. Egerton, Control of radiation damage in the TEM, *Ultramicroscopy* 127 (2013) 100–108.
- [33] P.D. Nellist, B.C. McCallum, J.M. Rodenburg, Resolution beyond the 'information limit' in transmission electron microscopy, *Nature* 374 (6523) (1995) 630–632.
- [34] T.J. Pennycook, G.T. Martinez, P.D. Nellist, J.C. Meyer, High dose efficiency atomic resolution imaging via electron ptychography, *Ultramicroscopy* 196 (2019) 131–135.
- [35] I. Lobato, D. Van Dyck, MULTEM: a new multislice program to perform accurate and fast electron diffraction and imaging simulations using Graphics Processing Units with CUDA, *Ultramicroscopy* 156 (2015) 9–17.
- [36] C.M. O'Leary, G.T. Martinez, E. Liberti, M.J. Humphry, A.I. Kirkland, P.D. Nellist, Contrast transfer and noise considerations in focused-probe electron ptychography, *Ultramicroscopy* 221 (2021), 113189.
- [37] P. Carra, B.T. Thole, Anisotropic x-ray anomalous diffraction and forbidden reflections, *Rev. Mod. Phys.* 66 (4) (1994) 1509.
- [38] V.E. Dmitrienko, Forbidden reflections due to anisotropic X-ray susceptibility of crystals, *Acta Crystallogr., Sect. A: Found. Crystallogr.* 39 (1) (1983) 29–35.
- [39] J.M. Cowley, A.F. Moodie, The scattering of electrons by atoms and crystals. I. A new theoretical approach, *Acta Crystallogr.* 10 (10) (1957) 609–619.